Journal of Materials Science & Technology 67 (2021) 135–144

Contents lists available at ScienceDirect

Journal of Materials Science & Technology

journal homepage: www.jmst.org

Research Article

Effect of sintering temperature on the chemical bonding, electronic structure and electrical transport properties of β-$Ga_{1.9}Fe_{0.1}O_3$ compounds

Swadipta Roy, C.V. Ramana *

Center for Advanced Materials Research (CMR), University of Texas at El Paso, El Paso, 500 W University Ave, El Paso, TX, 79968, United States

ARTICLE INFO

Article history:
Received 3 April 2020
Received in revised form 29 May 2020
Accepted 29 May 2020
Available online 26 July 2020

Keywords:
Ga_2O_3 compounds
Fe-doping
Raman spectroscopy
Chemical bonding
Electrical properties

ABSTRACT

A model system, which is based on iron (Fe) doped gallium oxide (Ga_2O_3) ($Ga_{1.9}Fe_{0.1}O_3$), has been considered to elucidate the combined effect of transition-metal ion doping and processing temperature on the chemistry, local structure and chemical bonding, and electrical transport properties of a wide band gap oxide (Ga_2O_3). The $Ga_{1.9}Fe_{0.1}O_3$ compounds were synthesized using standard high-temperature solid state reaction method. The effect of processing conditions in terms of different calcination and sintering environments on the structural and electrical properties of $Ga_{1.9}Fe_{0.1}O_3$ compounds is studied in detail. Structural characterization by Raman spectroscopy revealed that $Ga_{1.9}Fe_{0.1}O_3$ compounds exhibit monoclinic crystal symmetry, which is quite similar to the intrinsic parental crystal structure, though Fe-doping induces lattice strain. Sintering temperature (T_{sint}) which was varied in the range of 900−1200 °C, has significant impact on the structure, chemical bonding, and electrical properties of $Ga_{1.9}Fe_{0.1}O_3$ compounds. Raman spectroscopic measurements indicate the proper densification of the $Ga_{1.9}Fe_{0.1}O_3$ compounds achieved through complete Fe diffusion into the parent Ga_2O_3 lattice which is evident at the highest sintering temperature. The X-ray photoelectron spectroscopy validates the chemical states of the constituent elements in $Ga_{1.9}Fe_{0.1}O_3$ compounds. The electrical properties of $Ga_{1.9}Fe_{0.1}O_3$ fully controlled by T_{sint}, which governed the grain size and microstructural evolution. The temperature and frequency dependent electrical measurements demonstrated the salient features of the Fe doped Ga_2O_3 compounds. The activation energy determined from Arrhenius equation is ~0.5 eV. The results demonstrate that control over structure, morphology, chemistry and electrical properties of the $Ga_{1.9}Fe_{0.1}O_3$ compounds can be achieved by optimizing T_{sint}.

© 2021 Published by Elsevier Ltd on behalf of The editorial office of Journal of Materials Science & Technology.

1. Introduction

Oxide dielectrics which can exhibit enhanced thermal and chemical stability continue to attract the scientific and research community. The oxide based dielectric materials find interesting applications in all of the modern technological applications, which involve photocatalysis, chemical sensing, energy storage, and optoelectronics [1–3]. Gallium oxide (Ga_2O_3), one among the wide band gap oxides, exhibits quite interesting physical, chemical, electronic, optical and optoelectronic properties, which can be readily utilized in a multitude of technological applications [4,5]. With a band gap (E_g) of ~5 eV, Ga_2O_3 is an ideal candidate for utilization in the field of electronics [4,6], optoelectronics [7,8], spintronics [9,10], chemical sensing [11,12], and ultraviolet photo detectors [13,14]. Ga_2O_3 exhibits polymorphism; α-, β-, γ-, δ-, and ε- phases of Ga_2O_3 are widely known [15]. However, among these polymorphs, β-Ga_2O_3 is the most stable phase both chemically and thermally. Thin films and nanostructures of intrinsic and doped β-Ga_2O_3 are quite attractive for numerous technological applications [15].

While intrinsic β-Ga_2O_3 is listed as an insulating oxide, the electrical and photoconductivity of Ga_2O_3 can be modified to derive *n*-type semiconducting behavior by selective metal ions doping [14–17]. The reason behind this *n*-type semiconducting behavior can be attributed to the ionization of oxygen vacancies in Ga_2O_3 which is the main source of electrons. However, the electrical properties of both intrinsic and doped Ga_2O_3 compounds is still under debate which requires more deeper and fundamental studies [18,19]. "In fact, from this viewpoint, intrinsic and metal-

* Corresponding author.
E-mail address: rvchintalapalle@utep.edu (C.V. Ramana).

https://doi.org/10.1016/j.jmst.2020.05.072
1005-0302/© 2021 Published by Elsevier Ltd on behalf of The editorial office of Journal of Materials Science & Technology.

doped Ga_2O_3 materials have drawn the significant attention of many researchers in recent years [18–20]". Doping metal ions into Ga_2O_3 has been proved to be quite useful in designing electrodes for enhanced photo-catalytic activity [14,19,20]. The doped compounds are very tolerant and can be efficiently used under hostile environments of high pressure and temperature ($\geq$ 500 °C) for chemical sensing and catalysis [21,22].

The present work has been performed in order to understand the chemical bonding, structural quality and electrical properties of Fe doped Ga_2O_3 (GFO) materials. In addition to tuning the electrical properties, inclusion of specific transition metal (TM) ions into Ga_2O_3 is expected to show magnetic and magneto-electronic properties, which might be useful for integration into other future applications [9]. Therefore, from fundamental as well as applied perspective, it is interesting and highly beneficial to derive a better understanding of the underlying science of the TM- ion doping into Ga_2O_3 to design and develop materials for specific applications [21–23]. Furthermore, it is widely accepted in the literature that the sintering temperature influences the phase and chemical composition stability, microstructure, thermal and electrical properties of ceramics materials [24–28]. In this context, efforts in this work were fully directed to understand the effect of Fe doping on the chemical bonding, structural quality, and electrical properties of Ga_2O_3.

The reason for choosing Fe as a dopant into Ga_2O_3 is due to the following reasons. The chemical valence states of the Fe and Ga ions are similar in addition to the fact that the Shannon ionic radii for Ga and Fe in β-Ga_2O_3 and Fe_2O_3, respectively, are almost equal for both tetrahedral and octahedral positions [23]. Therefore, studying the Fe doping induced effect on the structural and functional properties of the GFO compounds will be quite interesting. Such studies may result in novel compounds with unique structural and functional properties for a wide variety of technological applications and/or enhanced performance in those optical, electronic and optoelectronic devices that currently benefit by the utilization of Ga_2O_3. However, the high-temperature processing conditions along with the optimum composition of the compound are the key to realize materials with desired properties and phenomena. Therefore, the high temperature synthesis conditions along with the exact Fe doping concentration considered for investigation and optimization studies. Note that it is quite evident in many cases that high temperature fabrication route can induce strain in lattice structure [29] and, thereby, alter the whole material system which may impact the final desired properties. Practically, although they are similar, the Shannon ionic radii of Fe is slightly higher than the Ga. Thus, if these two factors are combined, then massive lattice deformation may take place in case Fe concentration not maintained properly. Furthermore, emergence of mixed-valence states of cations and segregation of secondary phases of Fe oxides can also be anticipated with increasing sintering temperature and for low doping concentration which itself has an interesting impact on the structure-property relationship [23]. Therefore, and also based on our previous work on the set of GFO compounds with variable composition, a legitimate Fe doping concentration was chosen to study the influence of the above-mentioned factors.

The combined effect of processing conditions and alloying with Fe on the structure, chemistry and electrical properties of $Ga_{1.9}Fe_{0.1}O_3$ ceramics are reported in this paper. To examine the effect of Fe incorporation into Ga_2O_3 and understand the Fe-induced chemical bonding changes, X-ray photoelectron spectroscopy (XPS) coupled with Raman spectroscopy were employed. XPS combined with Raman spectroscopy helped us to comprehensively understand the intricacy of the chemistry associated with the Fe-doping and synthetic conditions of $Ga_{1.9}Fe_{0.1}O_3$. Understanding the crystallographic and chemical structural changes and correlating with electrical properties of these $Ga_{1.9}Fe_{0.1}O_3$ compounds are, thus, expected to further enhance our current understanding of the TM-ion alloying of Ga_2O_3.

2. Experimental details

2.1. Materials and synthesis of $Ga_{1.9}Fe_{0.1}O_3$ ceramics

Our approach to the synthesis of Fe-doped Ga_2O_3 ceramics by the high-temperature solid state chemical reaction method has been described elsewhere [23,30,31]. Briefly, the description of materials and synthetic procedures are as follows. Phase pure Ga_2O_3 (99.99 %) and iron (III) oxide (99.95 %) were obtained from Sigma Aldrich and Noah Technologies Corporation, respectively. These oxide powders were used as the precursor materials for preparing the GFO compounds. Polyvinyl alcohol (PVA) and ethanol were used as binders. Iron doped Ga_2O_3 was prepared by employing high temperature solid state reaction synthesis process. Precursor materials were weighed stoichiometrically and mixed according to the specified composition, i.e., x = 0.10. Finally, four distinct pellets were made to study the effects of calcination and sintering on the above-mentioned properties. Elaborated processing details can be obtained from our previous work reported elsewhere [23].

2.2. Characterization

2.2.1. X-ray photoelectron spectroscopy (XPS)

W We adopted the previously established procedures and methods to characterize intrinsic or doped Ga_2O_3 materials using XPS [31]. For clarity purpose, the details of XPS measurements and analytical procedures performed are as follows. XPS scan of the four differently sintered $Ga_{1.9}Fe_{0.1}O_3$ compounds were obtained employing Kratos Axis Ultra DLD spectrometer using Al *K*α monochromatic X-ray source (1486.6 eV). The survey and high-resolution (HR) scans were carried out at a pass energy of 160 and 40 eV, respectively. Survey scans and high-resolution spectra of Ga 2p, Fe 2p, O 1s, C 1s and Ga 3d peak regions were obtained analyzed to understand the effect of Fe doping into Ga_2O_3. The survey and high-resolution (HR) scans were carried out at a pass energy of 160 and 40 eV, respectively. Charge neutralizer was set to a value of 3.5 eV as these are insulating ceramic oxide samples. Raw XPS data were fitted with the help of CasaXPS software using Gaussian/Lorentzian (GL(30)) line shape and Shirley background correction. Survey scans were collected over the binding energy (B.E.) range of 1400-(-) 5 eV, whereas HR spectra of Ga 2p, Fe 2p, O 1s, C 1s and Ga 3d peak regions were obtained with at least 8 number of sweeps for each of them depending on the clarity of the peaks. Though both the Ga peaks (i.e., Ga 2p and 3d) were collected for confirmation, only Ga 2p spectra is depicted in order to avoid confusion coming from the interference of Ga 3d peak with O 2s peak as both the peaks are very closely situated. Detailed discussions on sample preparation techniques for XPS, precautions taken during sample transfer from the furnace atmosphere to the XPS analysis chamber and during XPS data collection, and particular instrumental parameters used for scanning can be found elsewhere [31]. Specifically, these procedures adopted were found to be efficient to evaluate both intrinsic and doped Ga_2O_3 compounds. The binding energy of carbon (C 1s) peak at 285 eV was used for charge referencing all other HR spectra. Estimation error of ±0.01 at.% was considered in order to obtain elemental concentration.

2.2.2. Raman spectroscopy

Raman spectroscopic studies were performed on an InVia Micro RAMAN (Renishaw) spectrophotometer with 532 nm laser excitation. The peaks were fitted following the standard procedure as

widely reported in the literature [32,33]. Briefly, Raman spectra were fitted by the superposition of the Lorentzian function:

$$I(\omega) = I_0 + \left(\frac{2A}{\pi}\right)\left(\frac{W}{W + 4(\omega - \omega_0)^2}\right) \quad (1)$$

where ω is phonon frequency of the peak, 'ω_0' is maximum phonon frequency of the peak, W is full width at half maxima (FWHM), 'A' is normalization constant, and 'I_0' is intensity of the background.

2.2.3. Electrical properties

The electrical measurements on the $Ga_{1.9}Fe_{0.1}O_3$ ceramics fabricated at various T_{sint} were carried out using HP precision LCR meter. Data were collected both at room temperature and by varying temperature in the range of 30–700 °C. The sample preparation techniques and precautions taken during electrical measurements were discussed elsewhere [25,27]. AC resistivity (ρ_{ac}) and conductivity of the samples were calculated as a function of temperature from the raw data. Each measurement was performed at least three times in order to check data reproducibility.

3. Results and discussion

3.1. Chemical structure and bonding

The Raman spectroscopic data of $Ga_{1.9}Fe_{0.1}O_3$ ceramics are shown in Fig. 1. The Raman spectroscopic data of $Ga_{1.9}Fe_{0.1}O_3$ ceramics are shown in Fig. 1(a), while the standard peak-fitting procedure employed to fit the data is represented in Fig. 1(b). To understand the effect of Fe doping, the expanded region of the Raman peak corresponding to Fe-O bonding is presented separately in Fig. 1(c). It can be seen that the spectra exhibit several characteristics peaks, which are indicative of crystalline nature of the samples. Furthermore, the Raman scattering peak evolution with increasing T_{sint} is evident (Fig. 1(a)). The Raman spectra can be conveniently analyzed, based on the crystal structure and crystal symmetry considerations of Ga_2O_3, in order to understand the chemical quality and chemical bonding within $Ga_{1.9}Fe_{0.1}O_3$. The monoclinic β-Ga_2O_3 belongs to the space group C2/m/C32 h. According to factor group analysis [34], the crystal modes can be classified according to:

$$\Gamma_{opt} = 10A_g + 5B_g + 4A_u + 8B_u \quad (2)$$

where, symmetry A_g and B_g phonon modes are Raman active while phonon modes with A_u and B_u symmetry are infrared active. Thus, a total of 15 Raman modes and 12 infrared active modes are predicted for β-Ga_2O_3 [34–36]. The Raman scattering peaks observed in the present work and their mode assignments are presented in Table 1. The data obtained for $Ga_{1.9}Fe_{0.1}O_3$ sintered at various T_{sint} are presented and compared with that of bulk Ga_2O_3. The Raman-active modes of Ga_2O_3 can be classified into three groups: high-frequency stretching and bending of GaO_4 tetrahedra (~770–500 cm^{-1}), mid-frequency deformation of Ga_2O_6 octahedra (~480–310 cm^{-1}), and low-frequency libration and translation (below 200 cm^{-1}) of tetrahedra-octahedra chains [35,36].

The Raman peaks observed for $Ga_{1.9}Fe_{0.1}O_3$ ceramics sintered at T_{sint} = 1200 °C at 143, 168, 202, 345, 475, 652, and 763 cm^{-1} correspond to $B_g(2)$, $A_g(2)$, $A_g(3)$, $A_g(5)$, $A_g(7)/B_g(4)$, $A_g(9)/B_g(5)$, and $A_g(10)$ phonon modes, respectively [36]. The bands at lower frequencies are assigned to the librations and translations of chains. The bands at 413, 345, 320 cm^{-1} are assigned to the deformation of octahedron [36]. The bands at 763, 652, 629, 475 cm^{-1} are derived from the stretching and bending of tetrahedron [36]. The peak positions and mode assignments are in good agreement with

Table 1
Raman data for $Ga_{1.9}Fe_{0.1}O_3$ ceramics at various T_{sint}. The data of $Ga_{1.9}Fe_{0.1}O_3$ ceramics is compared with that of bulk Ga_2O_3.

Serial No.	Mode Symmetry	Rao et al [29].		This Work (Sintering Temperature) (°C)									
		Bulk Empirical Calculation (cm^{-1})	Bulk Experimental Data (cm^{-1})	900 (cm^{-1})	Frequency Shift (cm^{-1})	1000 (cm^{-1})	Frequency Shift (cm^{-1})	1100 (cm^{-1})	Frequency Shift (cm^{-1})	1200 (cm^{-1})	Frequency Shift (cm^{-1})
1	A_z	104	–	–	–	–	–	–	–	–	–
2	B_z	113	–	112	–	112	–	112	–	–	–
3	B_z	150	144	140	–4	143	–1	143	–1	140	–4
4	A_z	166	169	165	–4	165	–4	168	–1	168	–1
5	A_z	207	200	196	–4	196	–4	202	+2	199	–4
6	A_z	317	317	–	–	317	0	320	+3	317	0
7	A_z	348	344	342	–2	345	+1	345	+1	343	–1
8	B_z	356	–	–	–	–	–	–	–	–	–
9	A_z	414	416	413	–3	413	–3	413	–3	412	–4
10	A_z	469	472	–	–	472	0	–	–	472	0
11	B_z	474	–	–	–	–	–	475	+1	–	–
12	A_z	601	629	611	–18	–	–	–	–	–	–
13	B_z	624	–	–	–	627	–	627	–	622	–
14	A_z	635	654	652	–2	649	–5	652	–2	655	+1
15	A_z	732	767	754	–13	760	–7	763	–4	763	–4

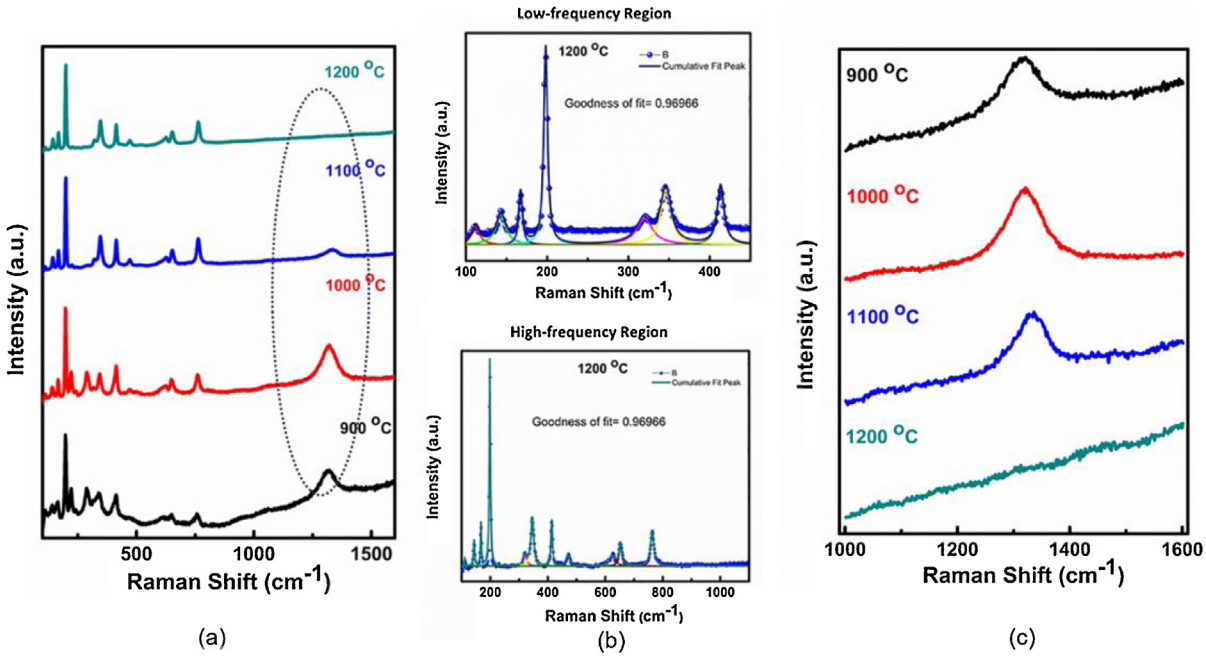

Fig. 1. (a) Raman spectra of differently sintered GFO compounds. (b) Representative case of Raman spectral peak-fitting procedure. The data shown are for GFO sample sintered at 1200 °C. The peak fitting procedure has been indicated for different frequency regions of the spectrum collected. (c) Expanded region of the Raman peak corresponding to Fe-O bonding. It is evident that the sintering temperature strongly influences the evolution of Fe-O bonds in GFO compounds. The peak corresponding to Fe-O bonding completely disappears for the samples sintered under optimum sintering temperature.

those reported for β-Ga_2O_3 bulk. In addition, these observations and Raman mode assignments of the peaks are also in agreement with those reported for β-Ga_2O_3 thin films and nanowires [34–37].

The combined effect of Fe doping and processing conditions (T_{sint}) on the structural quality and chemical bonding in $Ga_{1.9}Fe_{0.1}O_3$ ceramics can be understood as follows. With Fe content, the Raman active modes of $Ga_{1.9}Fe_{0.1}O_3$ ceramics have a clear shift (see, Table 1). In addition, the Raman scattering peaks in the spectra also exhibit a line broadening (Fig. 1(a)) for $Ga_{1.9}Fe_{0.1}O_3$ ceramics. However, this is more dominant at lower T_{sint}. The broadening of the Raman peaks is clearly seen at T_{sint}=900 °C; the peaks continue to be broader until T_{sint}=1100 °C, at which point the peaks become sharp. Also, this peak broadening is particularly true for the Raman modes in the low-to-mid spectral range between 300 and 500 cm^{-1}, which is due to Fe atoms entering into the crystal lattice of Ga_2O_3 to form the $Ga_{1.9}Fe_{0.1}O_3$ ceramics. Such peak broadening in Raman modes due to dopant effects was also noted in β$(GaAl)_2O_3$ films, where the broadening of Raman modes was particularly dominant in the mid-spectral range with Al-doping [38]. The peak around 1400 cm^{-1} is vanishing as the sintering temperature has been increased which is shown by dotted circling in Fig. 1(a). Wang et al. reported that, with the increase of Al content, the Raman active modes of $(AlGa)_2O_3$ films exhibited a right shift coupled with a line broadening, especially at higher Al content [38]. This peak broadening of Raman modes in the 310–480 cm^{-1} range was attributed to the more Al atoms entering into the crystal lattice of Ga_2O_3 to form ternary solid solution [38]. However, the broadening observed in this case of Fe is not significant compared to Al in Ga_2O_3 due to the reason that Fe doping concentration is very less as well as ionic radii mismatch between Ga^{3+} and Fe^{3+} is very small [23,30,31,39].

The Raman spectroscopic data and analyses are in corroboration with our previous XRD and SEM results, which were discussed quite extensively in our previous work [23]. However, in the context of understanding the importance of present work, we describe the salient features here. Phase purity of all the synthesized GFO compounds were confirmed from X-ray diffraction (XRD) patterns [23]. XRD data, high resolution scans as well as refinement procedures revealed that all the GFO compounds were phase pure without any secondary phases [23,30]. For the specific composition in question i.e., $Ga_{1.9}Fe_{0.1}O_3$, it is evident from the XRD data that there is no secondary phase formation at any of the T_{sint} values. However, although not significant, a slight positive shift of the peak position with increasing T_{sint} can be noted. Thus, increasing T_{sint} induces a reduction in the interplanar distance between the crystal planes. This in turn induces some amount of strain in the crystal which may be due to Fe doping or excess thermal energy [23]. The effect of T_{sint} was not very significant; grain size varied in the range of ~55–64 nm with T_{sint}. However, the strain values increased gradually with increasing sintering temperature. The major effect of T_{sint} is the drastic decrease in porosity, which approaches minimum when the optimum T_{sint} = 1200 °C is used for synthesis of $Ga_{1.9}Fe_{0.1}O_3$ samples [23]. Also, because of the difference in the ionic radii of Fe^{3+} and Ga^{3+} and Fe^{3+} (0.64 Å) has smaller ionic radius than Ga^{3+} (0.76 Å), so iron doping will facilitate the formation of smaller nuclei during synthesis process. Incorporation of Fe in Ga_2O_3 may inhibit the grain growth during sintering process [23]. Combining the XRD studies with present Raman spectroscopic data, it is evident that the sintering temperature strongly influences the structural quality and evolution of Fe-O bonds in Fe-doped Ga_2O_3 compounds. The peak corresponding to Fe-O bonding completely disappears (Fig. 1(c)) for the samples sintered under optimum sintering temperature.

3.2. Surface chemistry and electronic properties

The XPS survey and deconvoluted core level spectra (Ga 2p, Fe 2p and O 1s) of $Ga_{1.9}Fe_{0.1}O_3$ ceramics are shown in Figs. 2 and 3, respectively. The Ga 2p and O 1s peaks are labelled in the survey spectra, but Fe concentration is so less that it can't be observed throughout the spectra, though high resolution XPS spectra evidenced the presence of Fe. The peak assignments were done after comparing with the binding energy (BE) following the standard

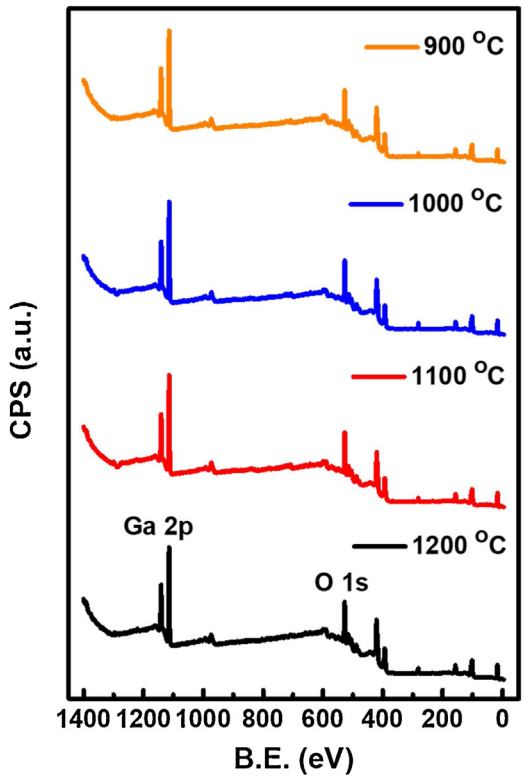

Fig. 2. Survey spectra of $Ga_{1.9}Fe_{0.1}O_3$ ceramics at various sintering temperature.

NIST database [40]. The Ga 2p region (Fig. 3(a)) combination of Ga 2p doublet i.e., the Ga $2p_{3/2}$ and Ga $2p_{1/2}$ peaks, which are located about at BEs of 1117.34 and 1144.17 eV, respectively. For the pure Ga metal, the location of Ga $2p_{3/2}$ is around 1116.50 [30,31,41,42]. Compared to the Ga metallic state, the observed Ga $2p_{3/2}$ peak shows almost 1 eV positive shift corroborating that all the Ga exists in the oxidation states. Ga 3d peak was also recorded (not shown) at a BE of 20.3 eV. This exhibited positive shift in the BE of Ga $2p_{3/2}$ peak is owing to the redistribution of the electronic charge, as Ga stabilized as Ga_2O_3 in the $Ga_{1.9}Fe_{0.1}O_3$ ceramics. The Ga 2p XPS data, which are consistent with the reported values in the literature for Ga_2O_3, validates the claim that Ga ions exist in the highest valence states (i.e., Ga^{3+}) in all the $Ga_{1.9}Fe_{0.1}O_3$ ceramics [43].

Fig. 3(b) depicts the HR XPS spectra of Fe 2p region. The deconvoluted spectra of Fe 2p region clearly reveals that Fe exhibits mixed valance state (i.e., Fe^{3+} at 711 eV and Fe^{2+} at 708.7 eV) for 1100 °C and 1200 °C sintered samples whereas single valance state (i.e., Fe^{3+}) of Fe exists for rest of the sintered samples [40]. It can be related to the varying diffusion rate associated with the electronic flux as sintering temperature approaches the optimized condition. This will help to achieve many unique as well as important characteristic properties such as magnetic, spintronic, and optical etc. out of the $Ga_{1.9}Fe_{0.1}O_3$ ceramics as a result of jumping and sharing of electronic clouds between these two valence states.

Finally, we consider the O 1s peak to further establish the surface chemistry and electronic structure while the BE values and full width at half maximum (FWHM) of all the elements are listed and compared in Tables 2 and 3. The O 1s peak (Fig. 3(c)), at a BE of 530.87 eV, is the characteristic feature of Ga-O bond [31,41,42]. The O 1s peak is not symmetric for all the sintered compounds. The HR core level spectra fitting mainly results in three components representing different chemical states. The most intense peak centered at B.E. of 530.25 eV is the characteristic peak of oxygen bonded to Fe within the GFO compound [31,41]. The third component located at higher BE (i.e., 532 eV), attributing to either carbonyl (oxygen bonded to carbon) or hydroxyl (oxygen bonded to hydrogen) groups, which were adsorbed on the sample surface as impurities during sample handling, appear as a shoulder contribution with minor intensities [43]. It can be noticed from O 1s spectra (Fig. 3(c)) that as the sintering temperature approaches optimized condition the contributions from Ga_2O_3 and iron oxides are levelling off. In 900, 1000 and 1100 °C sintered samples the iron oxide contribution is quite higher than the Ga_2O_3. This has happened because the precursor iron (III) oxide powder used for preparing these $Ga_{1.9}Fe_{0.1}O_3$ ceramics, was not well diffused through the system and dispersed mainly around the surface due to inefficient firing condition. Moreover, being a surface sensitive technique, XPS easily catches those iron oxide signals and as a result the iron oxide intensity came up as higher than the Ga_2O_3. With increasing sintering temperature, these excess undissolved iron (III) oxide compacts on the surface diffused through the bulk and intensity of iron oxide came down subsequently. The BE values of all the elements are listed and compared in Table 2.

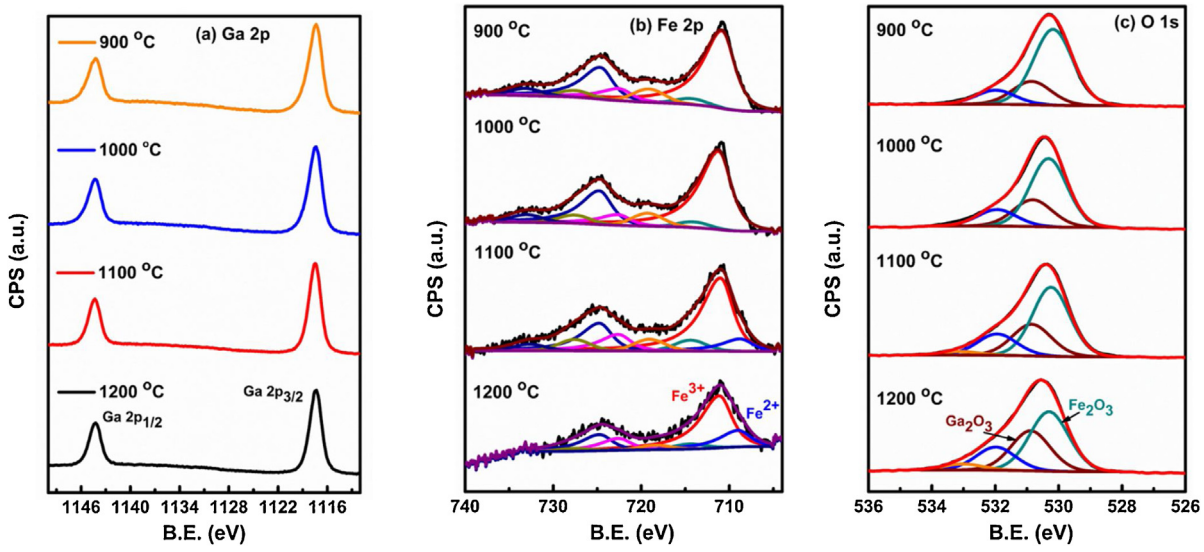

Fig. 3. Deconvoluted high-resolution XPS spectra of (a) Ga 2p, (b) Fe2p, and (c) O 1s.

Table 2
Comparison of B.E. of Ga 2p, O 1s and Fe 2p core level spectra of $Ga_{1.9}Fe_{0.1}O_3$ ceramics prepared under various sintering temperatures.

Sintering Temperature (°C)	Binding Energy (B.E.) (eV)				
	Ga $2p_{3/2}$ (Ga_2O_3)	O 1 s (Fe_xO_y, Ga_2O_3)		Fe $2p_{3/2}$ (Fe_xO_y)	
		Fe_xO_y	Ga_2O_3	FeO	Fe_2O_3
900	1117.34	530.21	530.87	–	710.94
1000	1117.35	530.25	530.83	–	711.10
1100	1117.35	530.29	530.87	708.71	711.06
1200	1117.37	530.25	530.86	708.76	711.00

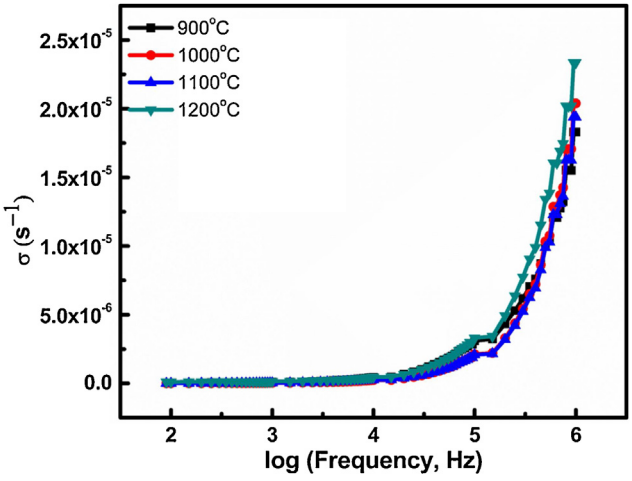

Fig. 4. Frequency dependent room-temperature ac conductivity of $Ga_{1.9}Fe_{0.1}O_3$ ceramics sintered at different conditions. Conductivity variation is not significant throughout the whole frequency range while increasing trend can be noticed at higher frequency level.

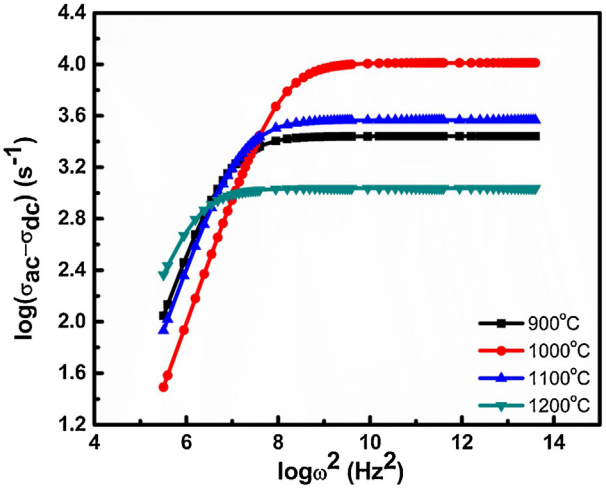

Fig. 5. $\log(\sigma_{ac}-\sigma_{dc})$ versus $\log \omega^2$ plots for $Ga_{1.9}Fe_{0.1}O_3$ ceramics. The initial linear plots are evident of small polaron hopping mechanism.

3.3. Electrical properties

The frequency dependent ac electrical conductivity (σ_{ac}) of the $Ga_{1.9}Fe_{0.1}O_3$ ceramics measured at room temperature are represented in Fig. 4. It is evident from the plots that the conductivity values are almost constant at lower frequency and more or less similar for all the $Ga_{1.9}Fe_{0.1}O_3$ ceramics sintered at different temperatures throughout the whole frequency range. However, after 10 kHz, the conductivity rapidly increases with increasing frequency. T_{sint} merely has any influence on the ac conductivity, though $Ga_{1.9}Fe_{0.1}O_3$ ceramics sintered at 1200 °C registered slightly higher conductivity than the other samples. The fundamental reason behind the sudden rise in ac conductivity is the hopping of electrons between multivalent cations. Hopping of charge carriers increases with the applied frequency which in turn increases the conductivity [44,45]. In order to derive a better understanding of this phenomenon as well as the validation of hopping mechanism, $\log(\sigma_{ac}-\sigma_{dc})$ versus $\log \omega^2$ plots were constructed. The data is shown in Fig. 6. All the plots show an initial linear behavior, which is an indication of small polaron mechanism [44–46] of electrical conduction in these samples. The mechanism can be explained with the help of the following equation [45]:

$$\sigma_{ac}-\sigma_{dc}=\omega^2\tau/(1+\omega^2\tau^2) \quad (3)$$

where, ω is the angular frequency and average relaxation time is denoted by τ. Therefore, for $\omega^2\tau^2 < 1$, $\log(\sigma_{ac}-\sigma_{dc})$ versus $\log\omega^2$ should display a linear behavior if conduction occurs by the small polar hopping mechanism in localized neighborhood [45]. It is clear from the plots presented in Fig. 5 that $\log(\sigma_{ac}-\sigma_{dc})$ versus $\log \omega^2$ yields linear plots for all the sintered samples which satisfies the polaron hopping theory requirements. Note that the polaron is a self-stabilized electronic charge in a deformable polar medium; the slow motion of polaron associated with lattice distortion is known as polaron hopping [46]. It is noted that the $Ga_{1.9}Fe_{0.1}O_3$ ceramics sintered at 1000 °C show a long linear region than the other samples. However, other $Ga_{1.9}Fe_{0.1}O_3$ ceramics display a legitimate linear portion before they achieve the saturated state.

Electrical conductivity of a material system, whether it is as a function of frequency or temperature, depends on certain factors, such as microstructure, chemistry, presence of defects, doping concentration, and fabrication method employed [45–47]. We reported previously, in a different study, that with increasing sintering temperature from 900 °C to 1200 °C, the effective density of the GFO compounds changes slightly while the relative porosity count decreases around 10 % [23]. The integration and annexation of the smaller grains is the main reason behind the porosity decline which eventually leads to continuous grain growth. As the sintering temperature has been increased, the grains received enormous kinetic energy for the grain boundary movement in the form of thermal energy and subsequently smaller grains coalescence to form larger grains. Additionally, Fe doping also served as the nucleating centers for the small grains [23]. Uniform particle distribution due to proper grinding enhanced the sintering efficiency. Combining these all factors help to achieve optimum porosity level with desired density of the GFO compounds at 1200 °C sintering temperature.

Doping in pure Ga_2O_3 causes segregation of the dopants at the grain boundary which acts as a barrier for grain growth during sintering process. Strong charge localization which leads to small polaron effect and hopping of electrons also influences electrical conductivity. Presence of excess localized charge carriers and their free movement under the influence of external (i.e., thermal) factors alter the unit cell structure by reshaping ionic bonding that can cause local distortion [46]. Lattice distortion impedes the movement of the free carriers by trapping them inside and as a result

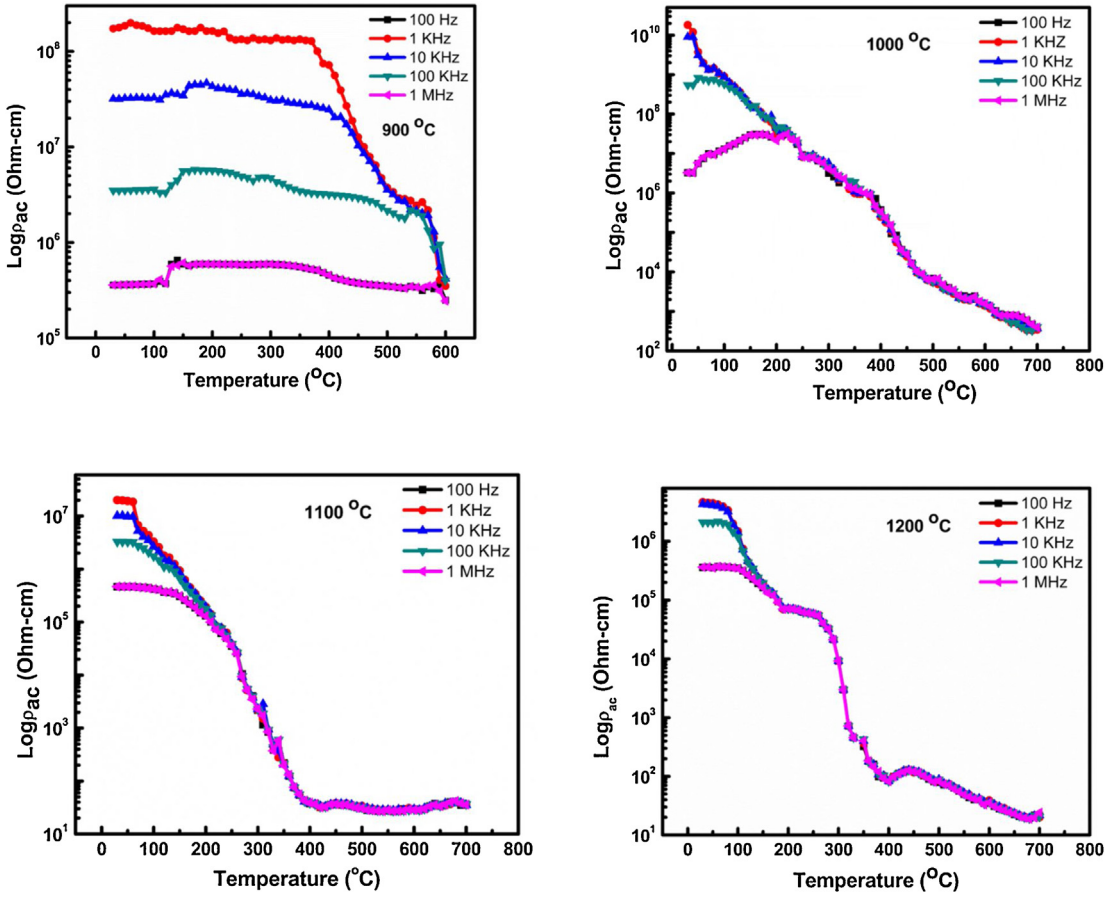

Fig. 6. Variation of ac electrical resistivity with temperature at different frequencies. The data shown are for $Ga_{1.9}Fe_{0.1}O_3$ ceramics sintered at above mentioned temperatures. It can be seen that ac resistivity decreases continuously with increasing sintering temperature.

electrical resistivity goes up sometimes. However, the room temperature resistivity can be expressed through Eq. (3):

$$\rho \propto (1/n\tau) \tag{4}$$

where, n represents the carrier's density and τ is relaxation time [44]. Sintering conditions have two major impacts on the room temperature resistivity; first τ decreases because of lattice distortion and the second is increase in the carrier concentration. At low sintering temperature, lattice parameter change owing to distortion is small; so, it is insignificant to consider the change in τ value. Thus, conductivity can only be increased by increasing the carrier concentration and an appropriate rise in temperature can generate more free electrons [44]. Although, higher temperatures or longer sintering durations can significantly change the lattice constants which further decreases τ leading to a decrease in conductivity [44].

Activation energy of the charge transport process must also be considered since it is responsible for the temperature dependent dc electrical characteristics. Activation energy of highly electrical resistive material is quite high [48]. At low temperature, free movement of charge carriers are constrained by both grain and grain boundaries; but, at higher temperatures, activation energy decreases due to the higher thermal energy and so the charge carrier gains mobility. Also, at high temperatures, grain boundary scattering is less, and the drift mobility of the carriers becomes enhanced leading to higher conductivity. Thermally activated behavior of charge carriers of differently sintered $Ga_{1.9}Fe_{0.1}O_3$ ceramics can be witnessed in the Fig. 6, where the ac resistivity is plotted against temperature as a function of frequency. The resistivity and conductivity for all the $Ga_{1.9}Fe_{0.1}O_3$ ceramics were calculated with the help of the following equations [49]:

$$|Z| = (Z'^2 + Z''^2)^0.5 \tag{5}$$

$$\rho = (ZA)/t \tag{6}$$

$$\sigma = 1/\rho \tag{7}$$

where, Z' denotes the real part and Z'' is the imaginary part of the impedance value, the overall impedance of the ac circuit is expressed as Z, A is the area and t is the thickness of the pellets, and σ represents the ac conductivity. It is evident from Fig. 6 that, with increasing sintering temperature, ac resistivity continuously decreases i.e. conductivity increases.

At lower temperatures higher frequency shows lower ρ values; but, ρ is independent of frequency at higher temperature. The plots clearly illustrate the decreasing trend of resistivity with increasing temperature which is sharp for 1100 °C and 1200 °C sintered samples; but, in 900 °C and 1000 °C samples resistivity decreases slowly with rising temperature. A step can be seen in the temperature range of 100–150 °C for the sample sintered at 900 °C. The feature becomes more evident with increasing frequency. It can be explained considering the changes occurring in the local moieties of the GFO compound with increasing operational frequency. The scattering of the charge carriers by the grain boundary increases with increasing frequency and this effect cannot be ignored in compounds synthesized at substantially low temperatures. Though, the operational temperature has been increased sufficiently from the room temperature, but the frequency effect is prevalent in order to bring down the temperature impact. Also, the defect concentration in 900 °C sintered sample is quite high considering the other sam-

Table 3
Comparison of FWHM of Ga 2p, O 1s and Fe 2p core level spectra of differently sintered samples.

Sintering Temperature (°C)	FWHM				
	Ga $2p_{3/2}$ (Ga_2O_3)	O 1 s (Fe_xO_y, Ga_2O_3)		Fe $2p_{3/2}$ (Fe_xO_y)	
		Fe_xO_y	Ga_2O_3	FeO	Fe_2O_3
900	1.40	1.51	1.45	–	1.40
1000	1.40	1.49	1.47	–	1.43
1100	1.40	1.51	1.44	1.51	1.41
1200	1.40	1.50	1.48	1.50	1.42

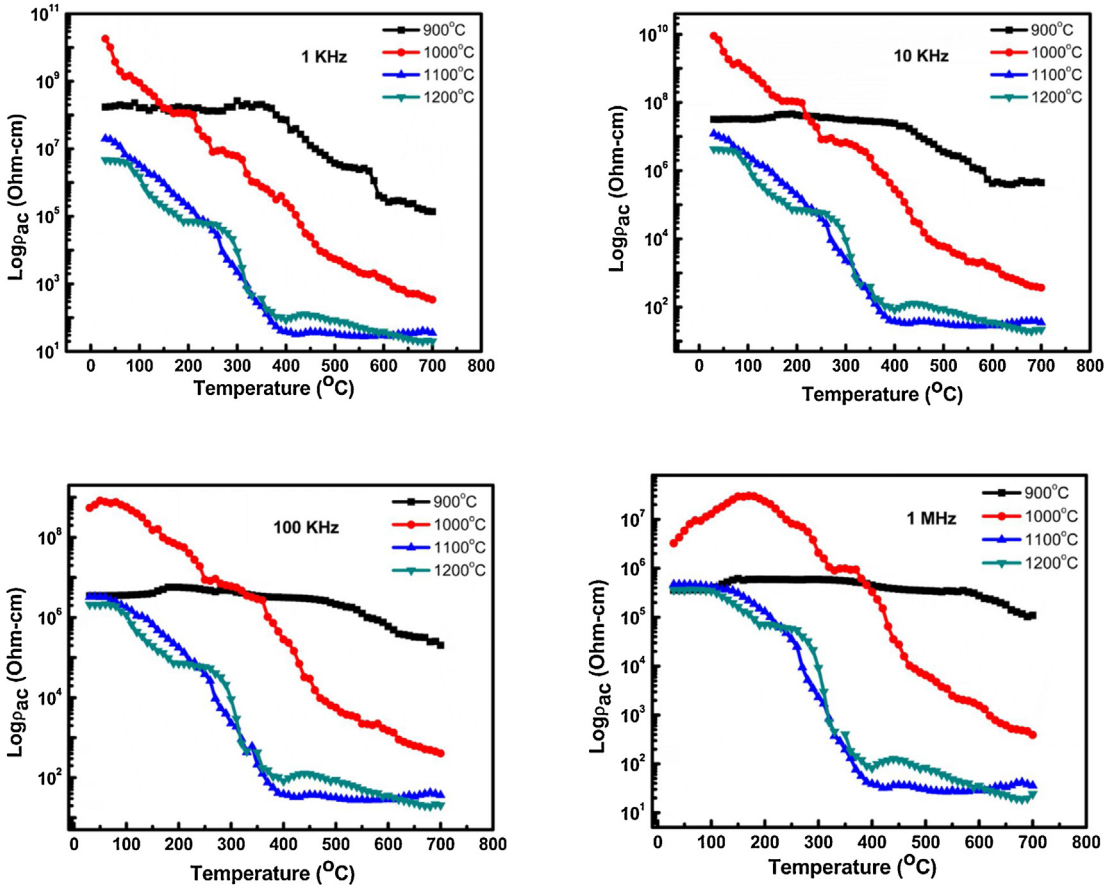

Fig. 7. Comparison of ac electrical resistivity of $Ga_{1.9}Fe_{0.1}O_3$ ceramics at various frequency.

ples. These small pockets of atomic defects combined together and contributed to the overall jump in the resistivity.

A sharp decline in the ρ value can be observed for 1100 °C and 1200 °C samples in the temperature region 200–400 °C. Generally, a legitimate concentration of defects such as interstitials, vacancy, anti-cites and foreign elements as dopants can affect the electrical conductivity [50–52]. This indicates that, at lower temperature, due to iron doping, there is a strong lattice-charge carrier interaction. Densely populated charge carriers may hinder their own movement by mutual trapping. At high temperature, free charge carriers and doped ions gain sufficient energy from the thermally activated processes. As a result, resistivity decreases with increasing temperature. Proper firing conditions have great impact on electrical conductivity, optical properties and mechanical properties. Intestinal oxygen atoms present in Ga_2O_3 act as a carrier trap and hinder the free movement of the charge carriers. Optimizing processing conditions reduces the amount of oxygen atoms present in the various interstitial positions and thus increases the conductivity and other properties [53]. With rising sintering temperature more interstitial oxygen vacancies were generated along with Ga^{3+}. Also, free electrons generated due to charge transfer between Fe^{2+} and Ga^{3+} and Fe^{3+}-Fe^{3+} double-excitation process which get released at conduction band and increased the electron density. As a result, carrier concentration has augmented which increased the overall conductivity. But, at very high sintering temperature, Ga_2O_3 may form solid solution with the iron oxide which can reduce the electron density. It is obvious that at lower sintering temperature, grain boundary diffusion activation energy is quite less. If sintering is not performed at high enough temperature, ceramics will not be able to achieve proper densification and the remained internal porosity will hinder the movement of the free carriers by scattering. Unwanted sintering condition may escalate the volatilization of Ga_2O_3. At optimized sintering temperature, defects and crystal boundaries get reduced; as a result, scattering decreases and mobility increases [44].

Temperature dependent electrical resistivity plots for differently sintered GFO samples are shown in Fig. 7. The data are shown at representative frequency values. It is evident from the figures that the electrical resistivity of 1100 °C and 1200 °C samples almost follow the same trend though the later one registered slightly less

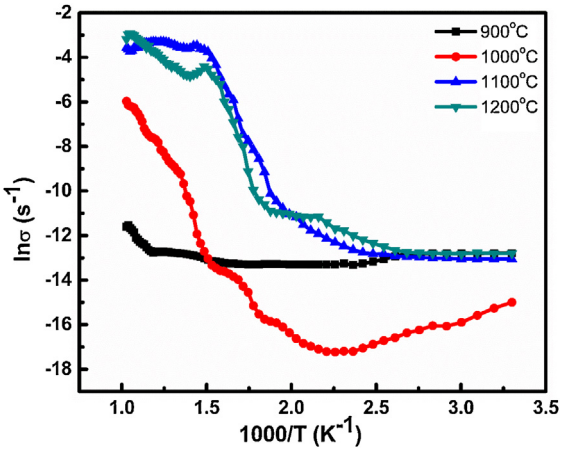

Fig. 8. Temperature dependent dc conductivity plot of $Ga_{1.9}Fe_{0.1}O_3$ ceramics sintered at different conditions.

resistivity value. Fig. 8 illustrates the absolute temperature dependent conductivity plots for all the samples at 1 MHz frequency. It is clear from the plot that conductivity increases with increasing sintering temperature. Though, the conductivity of 1000 °C sample was lower than the 900 °C sintered sample, but it surmounted the later at high temperature region consolidating the fact that with increasing sintering temperature densification occurs and porosity level decreases which in turn increases the conductivity. The 900 °C sintered sample shows almost constant conductivity throughout the experimental temperature range. The increment in conductivity with increasing temperature for 1100 °C and 1200 °C samples is quite manifold higher than the other two. Electron hopping and carrier mobility at the excited states are the main cause of this high temperature conductivity behavior which can be explained with the help of the following Eq. (7) [54]:

$$\sigma=\sigma_o\exp[-\Delta E_a/(k_BT)) \quad (7)$$

where, σ denotes the dc electrical conductivity, σ_o is a constant, activation energy is expressed as E_a, k_B is Boltzmann's constant, and T is the temperature in absolute scale. Activation energy of the samples were calculated with the help of the Arrhenius equation. The activation energy varied in the range of 0.59–0.45 eV with increasing sintering temperature. Fabrication method, impurity level, intrinsic crystal structure and atomic defects can have impact on the activation energy [54]. In the case of Fe-doped Ga_2O_3 samples as a function of sintering temperature, the highest activation energy (0.55 eV) is noted for sample sintered at 900 °C. This high activation energy at 900 °C may be due to incomplete calcination process which might have caused agglomeration of particles leading to carrier hindrance [53]. However, the activation energy values gradually decrease with increasing T_{sint} due to improved structural order and microstructure.

4. Conclusions

Raman spectroscopy validates that the differently sintered $Ga_{1.9}Fe_{0.1}O_3$ compounds crystallized in monoclinic crystal symmetry which is similar to the parent β-Ga_2O_3 crystal structure. Raman data qualitatively implicates about the lattice distortion of the parental phase due to Fe-doping and gives an overview on the final densification achieved which is driven by surface to bulk diffusion of the doping element. XPS study revealed that the samples show mixed or single valence states depending on the sintering condition. Moreover, stoichiometry of the constituent elements is verified employing the XPS analysis. By analyzing frequency and temperature dependent ac electrical conductivity data it is clear that small polaron and hopping mechanisms are the main dominating factors in the electrical transport behavior of Fe-doped Ga_2O_3. Sintering at 1200 °C enhanced free carrier movement to an optimized condition thereby recorded higher conductivity than the other samples. Activation energy calculation from the temperature dependent conductivity plot shows that 1200 °C sintered sample has the moderate activation energy of 0.46 eV. In conclusion, the firing condition explored for iron doped gallium oxide compounds have the potential for preparing functionalized nano-structured ceramic materials.

Acknowledgements

The authors acknowledge, with pleasure, support from the National Science Foundation (NSF) with grant # DMR-1827745. XPS measurements were performed at Environmental Molecular Sciences Laboratory (EMSL), a national scientific user facility sponsored by the Department of Energy's Office of Biological and Environmental Research and located at Pacific Northwest National Laboratory (PNNL), Richland, Washington.

References

[1] Y. Zhang, G. He, W. Wang, B. Yang, Y. Xia, J. Mater. Sci. Technol. 50 (2020) 1–12.
[2] W. Li, S. Qiu, N. Chen, G. Du, J. Mater. Sci. Technol. 26 (2010) 682–686.
[3] J.-Y. Baek, L.T. Duy, S.Y. Lee, H. Seo, J. Mater. Sci. Technol. 42 (2020) 28–37.
[4] R. Sun, H.Y. Zhang, G.G. Wang, J.C. Han, X.Z. Wang, L. Cui, X.P. Kuang, C. Zhu, L. Jin, Superlattices Microstruct. 65 (2014) 146–151.
[5] Y. Zhuo, Z. Chen, W. Tu, X. Ma, Y. Pei, G. Wang, Appl. Surf. Sci. 420 (2017) 802–807.
[6] R.K. Ramachandran, J. Dendooven, J. Botterman, S.P. Sree, D. Poelman, J.A. Martens, H. Poelman, C. Detavernier, J. Mater. Chem. A 2 (2014) 19232–19238.
[7] S. Hong, C.K. Rhee, Y. Son, J. Alloys. Compd. 774 (2017) 11–17.
[8] W. Xu, H. Cao, L. Liang, J.B. Xu, ACS Appl. Mater. Interfaces 7 (2015) 14720–14725.
[9] H. Hayashi, R. Huang, H. Ikeno, F. Oba, S. Yoshioka, I. Tanaka, S. Sonoda,Appl. Phys. Lett. 89 (2006), 181903.
[10] D. Guo, Z. Wu, Y. An, X. Li, X. Guo, X. Chu, C. Sun, M. Lei, L. Li, L. Cao, J. Mater. Chem. C 3 (2015) 1830–1834.
[11] C. Baban, Y. Toyoda, M. Ogita, Thin Solid Films 484 (2005) 369–373.
[12] J. Yu, L. Dong, B. Peng, L. Yuan, Y. Huang, L. Zhang, Y. Zhang, R. Jia,J. Alloys. Compd. 821 (2020), 153532.
[13] M. Orita, H. Ohta, M. Hirano, H. Hosono, Appl. Phys. Lett. 77 (2000) 4166–4168.
[14] W. Zhang, B.S. Naidu, J.Z. Ou, A.P. O'Mullane, A.F. Chrimes, B.J. Carey, Y. Wang, S.-Y. Tang, V. Sivan, A. Mitchell, K. Kalantar-Zadeh, ACS Appl. Mater. Interfaces 7 (2015) 1943–1948.
[15] F. Mezzadri, G. Calestani, F. Boschi, D. Delmonte, M. Bosi, R. Fornari, Inorg. Chem. 55 (2016) 12079–12084.
[16] M. Ogita, S. Yuasa, K. Kobayashi, Y. Yamada, Y. Nakanishi, Y. Hatanaka, Appl. Surf. Sci. 212 (2003) 397–401.
[17] Vu Thi Kim Oanh, Dong Uk Lee, Eun Kyu Kim, J. Alloys. Compd. 806 (2019) 874–880.
[18] M. Yamaga, E.G. Víllora, K. Shimamura, N. Ichinose, M. Honda,Phys. Rev. B 68 (2003), 155207.
[19] J.B. Varley, J.R. Weber, A. Janotti, C.G. Van de Walle,Appl. Phys. Lett. 97 (2010), 142106.
[20] Y. Sakata, Y. Matsuda, T. Yanagida, K. Hirata, H. Imamura, K. Teramura, Catal. Lett. 125 (2008) 22–26.
[21] R.R. Romanosky, S.M. Maley, Harsh Environment Sensor Development for Advanced Energy Systems, in: Micro- and Nanotechnology Sensors, Systems, and Applications V, Baltimore, MD(US), 2013, pp. 87250H.
[22] M. Fleischer, H. Meixner, Sens. Actuator B-Chem. 4 (1991) 437–441.
[23] S. Roy, C.V. Ramana, Inorg. Chem. 57 (2018) 1029–1039.
[24] H. Chen, H. Xiang, F. Dai, J. Liu, Y. Zhou, J. Mater. Sci. Technol. 35 (2019) 2778–2784.
[25] Z. Xu, M.A. Hodgson, P. Cao, J. Mater. Sci. Technol. 32 (2016) 1161–1170.
[26] Z. Cen, Y. Zhen, W. Feng, P. Zhao, L. Chen, X. Wang, L. Li, J. Eur. Ceram. Soc. 38 (2018) 3136–3146.
[27] S. Wu, X. Wei, X. Wang, H. Yang, S. Gao, J. Mater. Sci. Technol. 26 (2010) 472–476.
[28] Q. Zheng, H. Pan, J. Mater. Sci. Technol. 28 (2012) 920–926.
[29] L. Hu, X. Liu, H. Xie, J. Shen, T. Zhu, X. Zhao, Acta Mater. 60 (2012) 4431–4437.
[30] S. Roy, B. Mallesham, V.B. Zade, A. Martinez, V. Shutthanandan, S. Thevuthasan, C.V. Ramana, J. Phys. Chem. C 122 (2018) 27597–27607.
[31] B. Mallesham, S. Roy, S. Bose, A.N. Nair, S. Sreenivasan, V. Shutthanandan, C.V. Ramana, ACS Omega 5 (2020) 104–112.
[32] C.Y. Xu, P.X. Zhang, L. Yan, J. Raman Spectrosc. 32 (2001) 862–865.
[33] S.M. Ansari, B.B. Sinha, D. Phase, D. Sen, P.U. Sastry, Y.D. Kolekar, C.V. Ramana, ACS Appl. Nano Mater. 2 (2019) 1828–1843.

[34] T. Onuma, S. Fujioka, T. Yamaguchi, Y. Itoh, M. Higashiwaki, K. Sasaki, T. Masui, T. Honda, J. Cryst. Growth 401 (2014) 330–333.
[35] A. Khan, S.N. Khan, W. Jadwisienczak, M.E. Kordesch, Adv. Mater. 1 (2009) 236–240.
[36] R. Rao, A. Rao, B. Xu, J. Dong, S. Sharma, M. Sunkara,J. Appl. Phys. 98 (2005), 094312.
[37] Y. Zhao, R.L. Frost, J. Raman Spectrosc. 39 (2008) 1494–1501.
[38] X. Wang, Z. Chen, F. Zhang, K. Saito, T. Tanaka, M. Nishio, Q. Guo,AIP Adv. 6 (2016), 015111.
[39] R.D. Shannon, Acta Cryst. A. 32 (1976) 751–767.
[40] NIST X-ray Photoelectron Spectroscopy Database, NIST Standard Reference Database Number 20, NIST, Gaithersburg MD, 20899, 2000. (doi:10.18434/T4T88K).
[41] V. Zade, B. Mallesham, S. Roy, V. Shutthanandan, C.V. Ramana, ECS J. Solid State Sci. Technol. 8 (2019) Q3111–Q3115.
[42] M. Bandi, V. Zade, S. Roy, A.N. Nair, S. Seacat, S. Sreenivasan, V. Shutthanandan, C.G. Van de Walle, H. Peelaers, C.V. Ramana, Cryst. Growth Des. 20 (2020) 1422–1433.
[43] I. Lopez, A.D. Utrilla, E. Nogales, B. Mendez, J. Piqueras, A. Peche, J. Ramírez-Castellanos, J.M. González-Calbet, J. Phys. Chem. C. 116 (2012) 3935–3943.
[44] X. Mei, Y. Wang, L. Chen, C. Zhang, Y. Ma, Y. Zeng, Y. Jiang, Mat. Res. Innov. 19 (2015), S9-306-S309-309.
[45] D. Adler, J. Feinleib, Phys. Rev. B 2 (1970) 3112.
[46] E.J. Juarez-Perez, R.S. Sanchez, L. Badia, G. Garcia-Belmonte, Y.S. Kang, I. Mora-Sero, J. Bisquert, J. Phys. Chem. Lett. 5 (2014) 2390–2394.
[47] C.-C. Chen, C.-C. Chen, J. Mater. Res. 19 (2004) 1105–1117.
[48] M. El-Shabasy, J. Mag. Magn. Mater. 172 (1997) 188–192.
[49] M.T. Rahman, M. Vargas, C.V. Ramana, J. Alloys. Compd. 617 (2014) 547–562.
[50] A. Janotti, C.G. Van de Walle, J. Cryst. Growth 287 (2006) 58–65.
[51] A. Janotti, C.G. Van de Walle,Rep. Prog. Phys. 72 (2009), 126501.
[52] P. King, T.D. Veal, J. Phys,Condens. Matter 23 (2011), 334214.
[53] S. Du, Y. Tian, H. Liu, J. Liu, Y. Chen, J. Am. Ceram. Soc. 89 (2006) 2440–2443.
[54] M. Hashim, S. Kumar, S.E. Shirsath, E. Mohammed, H. Chung, R. Kumar, Physica B 407 (2012) 4097–4103.